separations

MDPI

Article

Chelation-Mediated Multicomponent Co-Assembly Strategy for Controllable Fabrication and Characterization of Titanium-Based Lithium-Ion Sieve with Selective Lithium Adsorption and Separation

Xia-Zhong Zhang [1,2], Guang-Ming Cheng [2], Yu-Ling Qiao [2], Xiong Tang [2], Shu-Ying Liu [2], Li-Yuan Zhang [2,3,*], Ting-Xing Zhao [1] and Hong-Bo Li [1,*]

[1] School of Materials and Chemistry, Southwest University of Science and Technology, Mianyang 621010, China; zhangxiazhong@163.com (X.-Z.Z.); tingxingzhao@swust.edu.cn (T.-X.Z.)
[2] School of Chemical and Environmental Engineering, Neijiang Normal University, Neijiang 641112, China
[3] Special Agricultural Resources in Tuojiang River Basin Sharing and Service Platform of Sichuan Province, Neijiang 641112, China
* Correspondence: zhangliyuansir@126.com (L.-Y.Z.); lihongbo@swust.edu.cn (H.-B.L.); Tel.: +86-832-2341577 (L.-Y.Z.)

Abstract

To address the growing demand for efficient and green recovery of lithium resources, this study develops a co-assembly strategy mediated by Ti(IV)/Li^+-polyacrylate complexes to fabricate mesoporous H_2TiO_3 lithium-ion sieve/carbon composites (H_2TiO_3@C), aiming to overcome the bottlenecks of conventional lithium-ion sieves such as large particle size, small specific surface area and limited adsorption capacity. Using tetrabutyl titanate (TBT, a Ti(IV) alkoxide precursor) and lithium acetate dihydrate as raw materials, a Ti(IV)/Li^+-polyacrylate complex is employed as a precursor, in which the carboxylate groups of polyacrylic acid coordinate to the titanium centers while Li^+ is ionically bound to the carboxylate groups; this complex co-assembles with poly(ethylene oxide)-poly(propylene oxide)-poly(ethylene oxide) (PEO-PPO-PEO) triblock copolymer (Poloxamer 188) to prepare Li_2TiO_3 mesoporous carbon composites (Li_2TiO_3@C). The results demonstrate that when the mass ratio of Li_2TiO_3 to polyacrylic acid and Poloxamer 188 is 1:2:0.3, the prepared lithium-ion sieve particles exhibit uniform morphology, a large specific surface area, significantly enhanced adsorption capacity, high selectivity for lithium adsorption, and good cycling stability. This work integrates chelation-mediated precursor design with co-assembly chemistry, providing a feasible pathway for the fabrication of mesoporous lithium-ion sieves.

Keywords: titanium-based lithium-ion sieves; polyacrylic acid; chelation-mediated; multicomponent co-assembly; lithium recovery

Check for updates

Academic Editor: Athanasia K. Tolkou

Received: 11 October 2026
Revised: 27 October 2026
Accepted: 29 October 2026
Published: 2 November 2026

Copyright: © 2026 by the authors. Licensee MDPI, Basel, Switzerland. This article is an open access article distributed under the terms and conditions of the Creative Commons Attribution (CC BY) license.

1. Introduction

Lithium, as a critical "energy metal" of the 21st century, not only provides sustained momentum for battery technologies and renewable energy sectors [1,2], but also plays a pivotal role in aerospace [3], metallurgy [4], nuclear industry [5,6], lubricants [7,8], ceramic and glass manufacturing [9], and refrigerants [10], earning it the name "white petroleum" in the new energy era. According to a report by the International Energy Agency (IEA), the global lithium demand reached 165 thousand tonnes in 2023 and is projected to surge

to 1326 thousand tonnes by 2040 [11]. Lithium resources are broadly categorized into primary and secondary types. Primary lithium resources include salt-lake brine, hard-rock (pegmatite), and clay-type (emerging) deposits, while secondary resources comprise spent lithium-ion batteries and lithium-bearing waste materials [12,13]. Among these, brine-hosted lithium accounts for over 60% of global lithium reserves [14]. Given that the majority of lithium resources are present in salt-lake brines, the extraction of lithium from aqueous sources has become an inevitable direction for industrial development and an emerging research frontier.

Numerous methods have been developed for lithium recovery from salt-lake brines, including adsorption [15–19], membrane separation [20–24], precipitation [25–27], solvent extraction [28–32], and electrochemical techniques [33–35]. Although precipitation is characterized by low cost, simple operation, and high technological maturity, it is only applicable to brines with low Mg/Li ratios; brines with high Mg/Li ratios require pre-treatment [26]. Solvent extraction offers high selectivity and recovery efficiency, and is suitable for brines with complex compositions and high Mg/Li ratios; however, it entails high costs, expensive extractants that require repeated regeneration, and complex operation with stringent control over pH and temperature, demanding high process stability. Membrane separation technologies feature low energy consumption and high product purity; nevertheless, they are susceptible to fouling and clogging by suspended solids and scaling substances in brines, necessitating rigorous pre-treatment, and are associated with substantial initial capital investment as well as high costs for membrane module replacement and maintenance. Electrochemical methods offer the advantages of chemical-free operation, environmental friendliness, high selectivity, and effectiveness for low-concentration lithium, but they face challenges in scale-up, high electrode material costs, low current efficiency, and are currently at the laboratory stage. In comparison with these approaches, adsorption offers high lithium adsorption capacity, strong anti-interference capability, recyclability of adsorbents, absence of toxic by-products, and operational simplicity. In particular, ion-exchange adsorption using lithium-ion sieves (LISs) has attracted increasing research interest due to its convenience, environmental compatibility, and excellent selectivity [36,37]. Lithium-ion sieves are generally classified into aluminum-based, manganese-based, and titanium-based types [38,39]. Compared with the former two, the titanium-based LISs exhibits superior structural stability [40], making it more widely adopted, with Li_2TiO_3 serving as the most common precursor for titanium-based LISs.

Although Li_2TiO_3-based titanium LISs have gained widespread application owing to their excellent stability, their adsorption performance still leaves room for further improvement. To date, modification strategies for LISs have primarily focused on composite fabrication and surface modification [41]. For instance, immobilizing lithium-ion sieves such as metatitanic acid (H_2TiO_3) onto high-specific-surface-area supports, exemplified by the HTO@BCA composite fabricated by combining HTO with biomass carbonaceous aerogel (BCA), affords a lithium equilibrium adsorption capacity of 39.8 $mg \cdot g^{-1}$, with the performance enhancement attributable to the synergistic improvement in specific surface area and hydrophilicity [42]. Using phenolic resin as a carbon precursor, Li_2TiO_3 was loaded onto porous carbon supports via an in-situ polymerization synchronous conversion method to increase both specific surface area and hydrophilicity, thereby elevating the adsorption capacity to 52.14 $mg \cdot g^{-1}$ [43]. Furthermore, the introduction of glycerol as an additive enables the preparation of ion sieves (LISs) with high specific surface area and abundant surface hydroxyl groups [44]. Alternatively, the incorporation of nitrogen-containing compounds such as cetyltrimethylammonium chloride (CTAC) enhances the specific surface area and surface roughness, both of which contribute to improved adsorption performance (the latter approach achieving a capacity of 49.05 $mg \cdot g^{-1}$) [45]. In addition, surface modification of

HTO via covalent grafting with the silane coupling agent (3-aminopropyl)triethoxysilane (APTES) can effectively prevent particle agglomeration, thereby optimizing the adsorption performance [46]. However, the aforementioned approaches, whether based on support loading or complex shaping processes, generally suffer from high fabrication costs, potential partial blockage of active sites on HTO by the supports, and limited increases in specific surface area.

Herein, we report a facile chelation-mediated multi-component co-assembly strategy for the controlled fabrication of Li_2TiO_3 nanocrystal@carbon composites. Specifically, a Ti(IV)/Li^+-polyacrylic acid complex was designed as a molecular precursor, which was synthesized by reacting tetrabutyl titanate ($Ti(OC_4H_9)_4$, a Ti(IV) alkoxide precursor) and lithium acetate dihydrate ($CH_3COOLi{\cdot}2H_2O$) with polyacrylic acid. In this system, polyacrylate serves as a carboxylate-rich ligand: its carboxylate groups coordinate to the titanium centers (forming Ti-OOCR linkages) and thereby moderate the hydrolysis/condensation of the Ti(IV) alkoxide, while Li^+ is ionically bound to the carboxylate groups through electrostatic association. Subsequently, the Ti(IV)/Li^+-polyacrylate complex was employed as a precursor co-assembled with Poloxamer 188 (P188) to yield Li_2TiO_3 mesoporous carbon composites (Li_2TiO_3@C). In this process, P188 acts as a structure-directing agent to form single micelles, onto which the Ti(IV)/Li^+-polyacrylate complex assembles into composite micelles (see Figure 1). The abundant carboxyl hydroxyl and carbonyl oxygen groups in the Ti^{4+}/Li^+-polyacrylate chelate can form hydrogen bonds with the hydroxyl groups in the PEO segments of Poloxamer 188 [47,48], enabling co-assembly. Through this chelation-mediated control of precursor composition, the Li and Ti precursors are uniformly dispersed at the solution/precursor stage, ultimately yielding a mesoporous LISs with small particle size, high specific surface area, and large adsorption capacity.

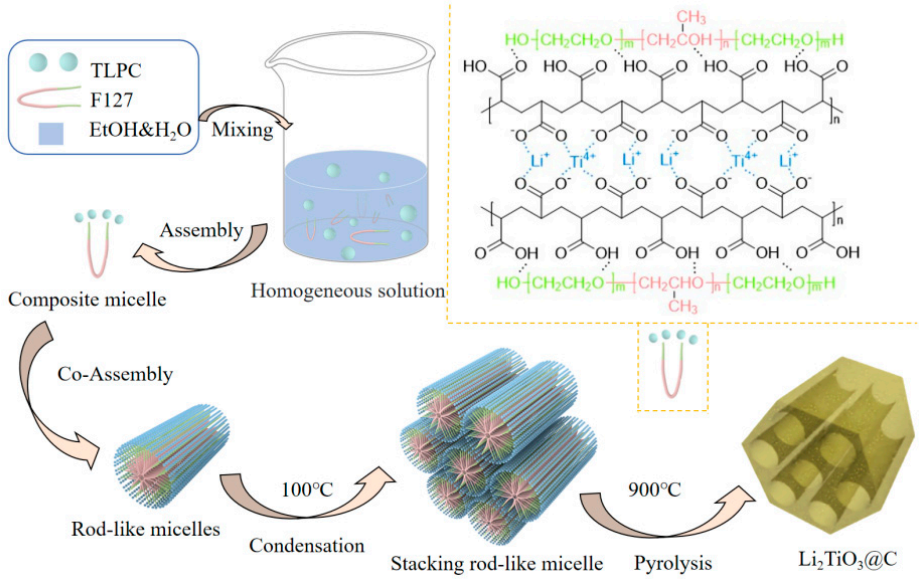


Figure 1. Schematic illustration of the chelation-mediated multi-component co-assembly process for constructing Li_2TiO_3@C.

2. Experimental Section

2.1. Reagents, Instruments, and Characterization

Reagents: Tetrabutyl titanate ($Ti(OC_4H_9)_4$, AR) was purchased from Anhui Zesheng Technology Co., Ltd., Anqing, China. Lithium acetate dihydrate ($CH_3COOLi{\cdot}2H_2O$, AR) was obtained from Shanxidong Xiya Chemical Co., Ltd., Linyi, China. Polyacrylic acid aqueous solution ($(C_3H_4O_2)_n$, 50 wt%) was supplied by Shanghai Aladdin Biochemical Technology Co., Ltd., Shanghai, China. Poloxamer 188 (P188, MW: 7680-9510) was pur-

chased from Bide Pharmatech Ltd., Shanghai, China. Lithium hydroxide monohydrate ($LiOH{\cdot}H_2O$, AR) was obtained from Xilong Scientific Co., Ltd., Shantou, China. Lithium chloride (LiCl, anhydrous, AR) was purchased from Bide Pharmatech Ltd., Shanghai, China. Anhydrous ethanol (C_2H_5OH), hydrochloric acid (HCl), and sodium hydroxide (NaOH) (all of analytical reagent grade) were supplied by Chengdu Kelong Chemical Co., Ltd., Chengdu, China.

Instruments: A muffle furnace (SX2-5-12TP) was purchased from Jinan Precision Scientific Instrument Co., Ltd., Jinan, China. X-ray diffraction (XRD) patterns were recorded on a DX-2700 diffractometer (Dandong Haoyuan Instrument Co., Ltd. Dandong, China). Scanning electron microscopy (SEM) was performed using a VEGA3 SBH instrument (TESCAN, Brno, Czech Republic). Field-emission scanning electron microscopy (FESEM) was conducted on a ZEISS Sigma 300 (Carl Zeiss AG, Oberkochen, Germany), equipped with a ZEISS SmartEDX energy-dispersive X-ray spectrometer (EDS, Carl Zeiss AG, Oberkochen, Germany). Atomic absorption spectrometry (AAS) was carried out on a WFX-200 instrument (Beijing Ruili Analytical Instrument Co., Ltd., Beijing, China). Inductively coupled plasma optical emission spectrometry (ICP-OES) was performed on an Optima 8000 instrument (PerkinElmer, Inc., Waltham, MA, USA). X-ray photoelectron spectroscopy (XPS) was recorded on an ESCALAB 250Xi spectrometer (Thermo Fisher Scientific Inc., Waltham, MA, USA). Nitrogen adsorption–desorption isotherms were measured using an ASAP 2460 surface area and porosity analyzer (Micromeritics Instrument Corporation, Norcross, GA, USA). Fourier-transform infrared (FT-IR) spectra were obtained on a WQF-510A spectrometer (Beijing Beifen-Ruili Analytical Instrument Co., Ltd., Beijing, China).

2.2. Experimental Methods and Procedures

2.2.1. Synthesis of Ti^{4+}/Li^{+}-Polyacrylate Chelates

Tetrabutyl titanate (17 mL, 50 mmol) and lithium acetate dihydrate (10.2 g, 100 mmol) were weighed separately in a molar ratio of 1:2 and each dissolved in 50 mL of anhydrous ethanol to obtain solutions A and B, respectively. Subsequently, according to the theoretical mass ratio of Li_2TiO_3 to polyacrylic acid of 1:x (x = 0, 1, 1.5, 2, 3), appropriate amounts of 50 wt% polyacrylic acid aqueous solution were weighed and designated as solutions C_0, C_1, C_2, C_3, and C_4, respectively. The C solutions were then added dropwise into solution A under stirring at 50 °C for 3 h to obtain solutions D, denoted as D_0, D_1, D_2, D_3, and D_4, respectively. Subsequently, solution B was added dropwise into solution D, and the mixture was continuously stirred at 45 °C for another 3 h, during which the ethanol was distilled off. Finally, the obtained gel was re-dissolved in water to afford the Ti^{4+}/Li^{+}-polyacrylate chelate (TLPC) solutions, which were successively denoted as T_0, T_1, T_2, T_3, and T_4.

2.2.2. Precursor Preparation: Synthesis of Li_2TiO_3 Mesoporous Carbon Composites (Li_2TiO_3@C)

Poloxamer 188 (P188) was weighed according to the theoretical mass ratio of Li_2TiO_3 to P188 of 1:z (z = 0, 0.1, 0.2, 0.3, 0.4), and then dissolved in a mixture of ethanol and water (16 mL, 4:1 v/v). The resulting solution was sequentially added to 50 mL of the T solutions, and the mixture was stirred at room temperature for 2 h. The obtained homogeneous solution was then poured into a Petri dish and kept at 40 °C for 8 h to evaporate the solvent, followed by continuous curing at 100 °C in an oven for approximately 20 h to completely remove the residual solvent, yielding the as-prepared P188/Ti^{4+}/Li^{+}/polyacrylate composite (denoted as PTLC). Subsequently, the as-prepared sample was pyrolyzed in a muffle furnace at 900 °C for 5 h with a heating rate of 2 °C min^{-1} to obtain the Li_2TiO_3@C lithium-ion sieve precursor, denoted as LTO. According to the increasing amounts of the

triblock copolymer Poloxamer 188 (P188) and polyacrylic acid, the samples were designated as LTO-n (n = 0, 1, 2, 3, 4), with LTO-0 serving as the control sample.

2.2.3. Ion Sieve Preparation: Acid Washing of Li_2TiO_3 Mesoporous Carbon Composites (Li_2TiO_3@C)

A 0.2 mol·L^{-1} hydrochloric acid solution was prepared for subsequent use. LTO-n samples (1 g each) were weighed into 250 mL Erlenmeyer flasks, and 100 mL of the hydrochloric acid solution was transferred into each flask. The acid washing was conducted in a water bath at 60 °C. At designated time intervals of 2, 4, 6, 8, 10, and 12 h, 4 mL of the supernatant was collected using a micropipette for analysis. After acid washing, the samples were collected by vacuum filtration, rinsed, and dried in an oven at 60 °C to obtain the ion sieves, denoted as HTO-n.

2.3. Lithium Adsorption

Effect of chelating agent dosage on the lithium adsorption capacity. HTO-n samples (100 mg each, n = 0, 1, 2, 3, 4) were weighed and placed into Erlenmeyer flasks containing 50 mL of LiCl solution with a concentration of 2 g·L^{-1}. The pH of the solution in each flask was adjusted to 12 using sodium hydroxide. Adsorption experiments were conducted at 298 K, and 4 mL aliquots of the supernatant were collected with a syringe every 2 h, during which the lithium ion concentration was determined by atomic absorption spectrophotometry. The equilibrium adsorption capacity was calculated using Equation (1):

$$Q_e = \frac{(C_0 - C_e)V}{m} \quad (1)$$

where Q_e (mg·g^{-1}) is the equilibrium adsorption capacity, C_0 (mg·L^{-1}) is the initial Li^+ concentration, C_e (mg·L^{-1}) is the equilibrium Li^+ concentration in solution, V (mL) is the volume of the adsorption solution, and m (g) is the mass of the lithium-ion sieve used.

Effect of pH on Adsorption Capacity. The pH of a 2 g·L^{-1} LiCl solution was adjusted using HCl and NaOH. Adsorption experiments were carried out at 298 K by adding 100 mg of HTO-3 to 50 mL of LiCl solution at various pH values (pH = 4, 7, 10, 11, 12). The remaining procedures were the same as described above.

Adsorption Isotherms. To obtain the adsorption isotherms at 298 K, 0.1 g of HTO-3 was added to 50 mL of LiCl solutions with different initial concentrations ranging from 100 to 450 mg·L^{-1}. The Langmuir and Freundlich models were applied using the following equations:

$$\frac{C_e}{Q_e} = \frac{1}{Q_m}C_e + \frac{1}{K_L Q_m} \quad (2)$$

$$\lg Q_e = \frac{1}{n}\lg C_e + \lg K_F \quad (3)$$

where Q_m (mg·g^{-1}) is the theoretical maximum adsorption capacity, K_L is the Langmuir constant, and K_F and n are the Freundlich constants.

Adsorption Thermodynamics. Based on the adsorption data at initial Li^+ concentration of 200 mg·L^{-1} at 298, 308, and 318 K, thermodynamic analysis was performed using the following equations:

$$K_d = \frac{C_0 - C_e}{m \times C_e} \times V \quad (4)$$

$$\ln K_d = \frac{\Delta S}{R} - \frac{\Delta H}{RT} \quad (5)$$

$$\Delta G = \Delta H - T\Delta S \quad (6)$$

where K_d ($mL \cdot g^{-1}$) is the distribution coefficient at a given temperature, ΔH ($kJ \cdot mol^{-1}$) is the enthalpy change, ΔS ($J \cdot mol^{-1} \cdot K^{-1}$) is the entropy change, ΔG ($kJ \cdot mol^{-1}$) is the Gibbs free energy change, and R (8.314 $J \cdot mol^{-1} \cdot K^{-1}$) is the ideal gas constant.

Adsorption Kinetics. At 298 K, 100 mg of HTO-3 was added to 100 mL of LiCl solution (C_{Li+} = 200 $mg \cdot L^{-1}$). During the adsorption process, aliquots of the mixed solution were taken at various time intervals to calculate the adsorption capacity. The time-dependent adsorption capacity curves were fitted using pseudo-first-order and pseudo-second-order models:

$$\lg(Q_e - Q_t) = \lg Q_e - \frac{k_1}{2.303} t \quad (7)$$

$$\frac{t}{Q_t} = \frac{1}{k_2 Q_e^2} + \frac{1}{Q_e} t \quad (8)$$

where Q_t ($mg \cdot g^{-1}$) is the adsorption capacity at time t, and k_1 and k_2 are the pseudo-first-order and pseudo-second-order rate constants, respectively.

Adsorption Selectivity. HTO-3 (50 mg) was added to 50 mL of a mixed cation solution containing Li^+ (1.55 $g \cdot L^{-1}$), Na^+ (3.15 $g \cdot L^{-1}$), and K^+ (0.25 $g \cdot L^{-1}$), [49]. The distribution coefficients $K_{d,Li}$ and $K_{d,M}$ were calculated using Equation (4), and the separation factor was determined by the following equation:

$$\alpha_M^{Li} = \frac{K_{d,Li}}{K_{d,M}} \quad (9)$$

where $K_{d,M}$ ($mL \cdot g^{-1}$) is the distribution coefficient of different metal ions.

Cyclic Adsorption Performance. Desorption of Li^+ from HTO-3 was conducted using 0.2 $mol \cdot L^{-1}$ HCl solution. The adsorption–desorption cycles were repeated five times (C_{LiCl} = 2 $g \cdot L^{-1}$).

3. Results and Discussion

3.1. Effect of Calcination Temperature on the Precursor

To investigate the influence of calcination temperature on the crystal structure of the material, a series of samples were prepared using the doping ratio of the LTO-3 sample. After aging and drying, the samples were calcined at 700 °C, 800 °C, 900 °C, and 1000 °C for 5 h, respectively. XRD analysis (Figure 2a) revealed that the crystal structures of the products obtained at different temperatures were highly consistent. Comparison with the standard card JCPDS 33-0831 confirmed that monoclinic Li_2TiO_3 was successfully synthesized at all four temperatures [46]. At 700 °C, only weak and broad diffraction signals can be detected, without sharp characteristic peaks of Li_2TiO_3, indicating that the solid-state reaction between lithium and titanium species is insufficient at this temperature. The monoclinic lithium metatitanate phase has not nucleated, and its crystal structure is not fully constructed; the sample is mainly amorphous precursor with extremely low crystallinity. As the calcination temperature increased from 700 °C to 900 °C, the intensities of the characteristic diffraction peaks increased significantly, with sharper peak shapes and gradually decreasing full width at half maximum (FWHM). These changes suggest an increase in crystallite size and improved crystal integrity. At a calcination temperature of 900 °C, the XRD peak intensities of all crystal planes of Li_2TiO_3 reached their maximum values, indicating that this temperature effectively promotes the complete development of the crystal structure, thus representing the optimal temperature for Li_2TiO_3 crystal growth.

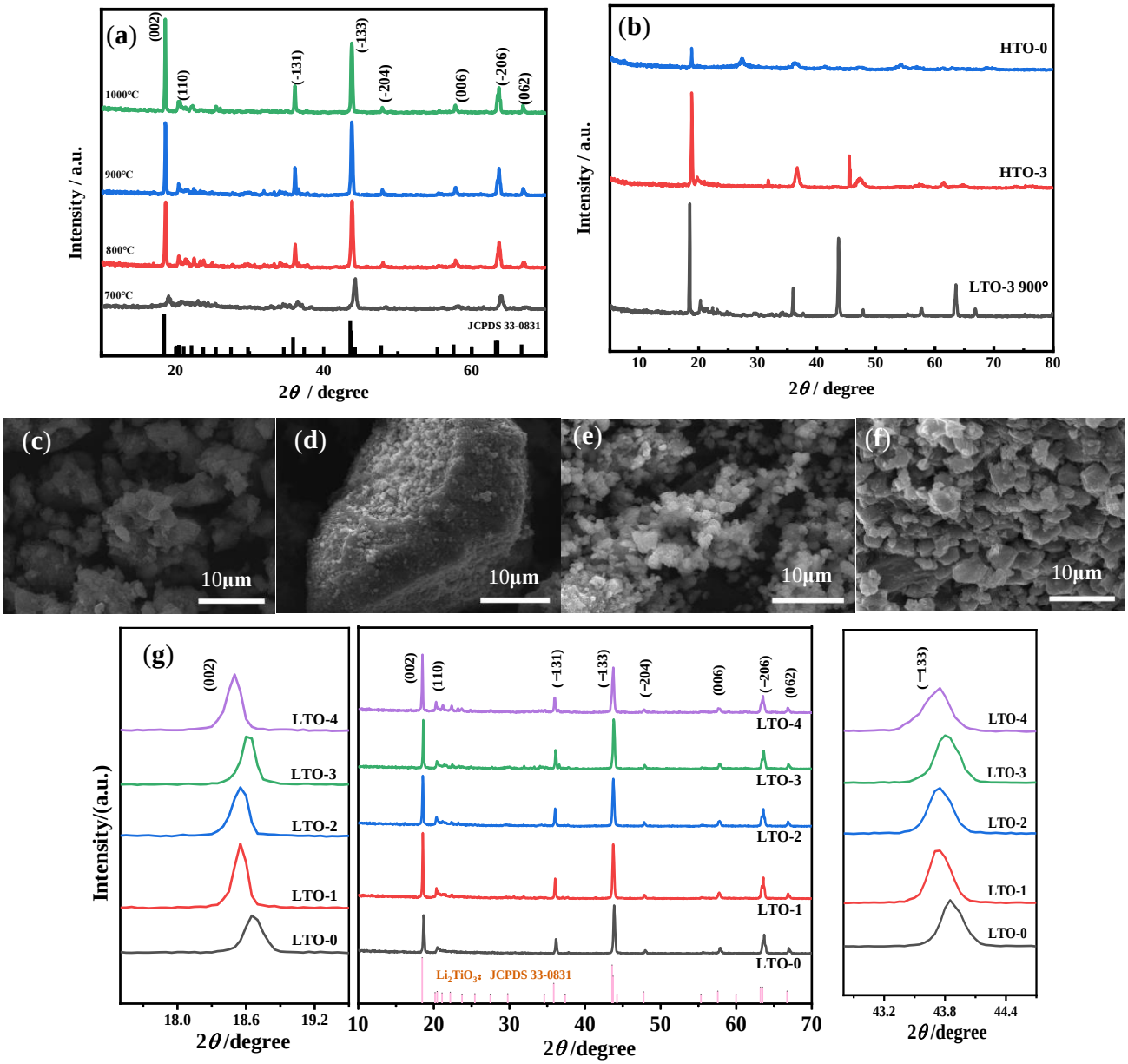


Figure 2. (**a**) XRD patterns of LTO-3 calcined at 700, 800, 900 and 1000 °C; (**b**) XRD patterns of LTO-3, HTO-3 and HTO-0; (**c**–**f**) SEM images of LTO-3 calcined at 700, 800, 900 and 1000 °C, respectively; (**g**) XRD patterns and partial enlarged view of LTO-n samples.

SEM was employed to examine the morphology of the Li_2TiO_3 samples prepared at different calcination temperatures, and the results are presented in Figure 2c–f. SEM observations revealed that the heat-treatment temperature significantly influenced the surface morphology of the materials. The sample prepared at 700 °C (Figure 2c) exhibited non-uniform particle sizes, with numerous fine particles agglomerated together, a rough block-like surface, and no discernible porous channels. When the temperature was raised to 800 °C (Figure 2d), the sample primarily consisted of large matrix particles with numerous nano-sized microcrystals attached to their surfaces, and well-defined pore structures had not yet developed. Upon increasing the temperature to 900 °C (Figure 2e), the particles became relatively uniform with no obvious agglomeration. Interparticle gaps emerged, giving rise to a highly uniform distribution of mesoporous structures. Further increasing the calcination temperature to 1000 °C (Figure 2f) resulted in fully grown grains with clear and regular grain contours, and the particle sizes were notably larger than those

sintered at 900 °C. The above morphological evolution is consistent with the XRD phase analysis results, collectively indicating that 900 °C is the optimal calcination temperature, under which well-crystallized and morphologically regular porous Li_2TiO_3 materials can be obtained.

3.2. Effect of Chelating Agent Mass Ratio on the Precursor

The XRD patterns of the precursors LTO-n (n = 0, 1, 2, 3, 4) prepared -with different chelating agent mass ratios are shown in Figure 2g. The characteristic diffraction peaks of the Li_2TiO_3 crystal structure are in good agreement with the standard pattern of Li_2TiO_3 (JCPDS No. 33-0831). The characteristic diffraction peaks of the Li_2TiO_3 crystal structure are in good agreement with the unit cell parameters of the standard Li_2TiO_3 card (JCPDS No. 33-0831). Specifically, the peaks at 18.57°, 35.96°, 43.78°, and 63.64° correspond to the (002), ($\bar{1}$31), ($\bar{1}$33), and ($\bar{2}$06) crystal planes of monoclinic Li_2TiO_3 in the C2/c space group, respectively [30], indicating that Li_2TiO_3@C composites with different formulations were successfully synthesized. The diffraction peaks of all samples were sharp with narrow full width at half maximum (FWHM) and high intensities, suggesting that the synthesized materials exhibit good crystallinity and well-developed crystal structures. This also demonstrates that the introduction of polyacrylic acid and P188 did not cause significant changes in the lattice structure of Li_2TiO_3. With increasing amounts of polyacrylic acid and P188, the diffraction intensity of the (002) crystal plane gradually increased, indicating that these two additives promoted preferential crystal growth along this plane. However, when the additive dosages were relatively high (e.g., LTO-3 and LTO-4), some weak impurity peaks appeared adjacent to the major diffraction peaks (e.g., the ($\bar{1}$31) crystal plane), which is mainly attributed to the amorphous carbon derived from the decomposition of excess chelating agents during the calcination process [50]. The introduction of chelating agents also induced changes in the unit cell volume and lattice parameters of Li_2TiO_3. As can be observed from the enlarged views of the (002) and ($\bar{1}$31) crystal planes in Figure 2g, the diffraction peaks of the modified samples shifted to lower angles with broadened profiles compared with those of the standard Li_2TiO_3 card. According to the Scherrer equation, the crystallite size was calculated to decrease [38,51]. Based on Bragg's law $2d \sin\theta = n\lambda$, the peak position is related to the interplanar spacing d. The shift toward lower angles (decrease in θ) indicates an increase in interplanar spacing (i.e., an increase in d), corresponding to lattice expansion. Such an enlarged interplanar spacing facilitates the diffusion of lithium ions [52]. Subsequent characterization and adsorption experiments further confirmed that LTO-3 exhibited the highest adsorption capacity.

As shown in Figure 2b, compared with the pristine LTO-3 before acid washing, the diffraction peaks of the (002) and ($\bar{1}$33) crystal planes of the acid-washed product HTO-3 shifted to higher angles. This confirms that the acid-washing-induced structural transformation is not fully reversible. Furthermore, Figure 2b reveals that the diffraction peak intensities of the modified HTO-3 are significantly higher than those of the unmodified HTO-0, indicating that the structural stability of the modified product is substantially enhanced.

Figure 3 presents the SEM images of the precursors LTO-n (n = 0, 1, 2, 3, 4). The SEM characterization results reveal that the lithium titanate precursors after carbon doping modification exhibit significantly optimized porous structural features. As shown in Figure 3a,b, the unmodified LTO-0 sample displays densely packed particles with relatively large particle sizes, a compact surface structure, and a paucity of pores. In contrast, the modified samples in Figure 3c–g show a marked increase in surface porosity, reduced particle sizes, and more uniform particle distribution, demonstrating that doping modification can effectively tailor the pore structure of the material.

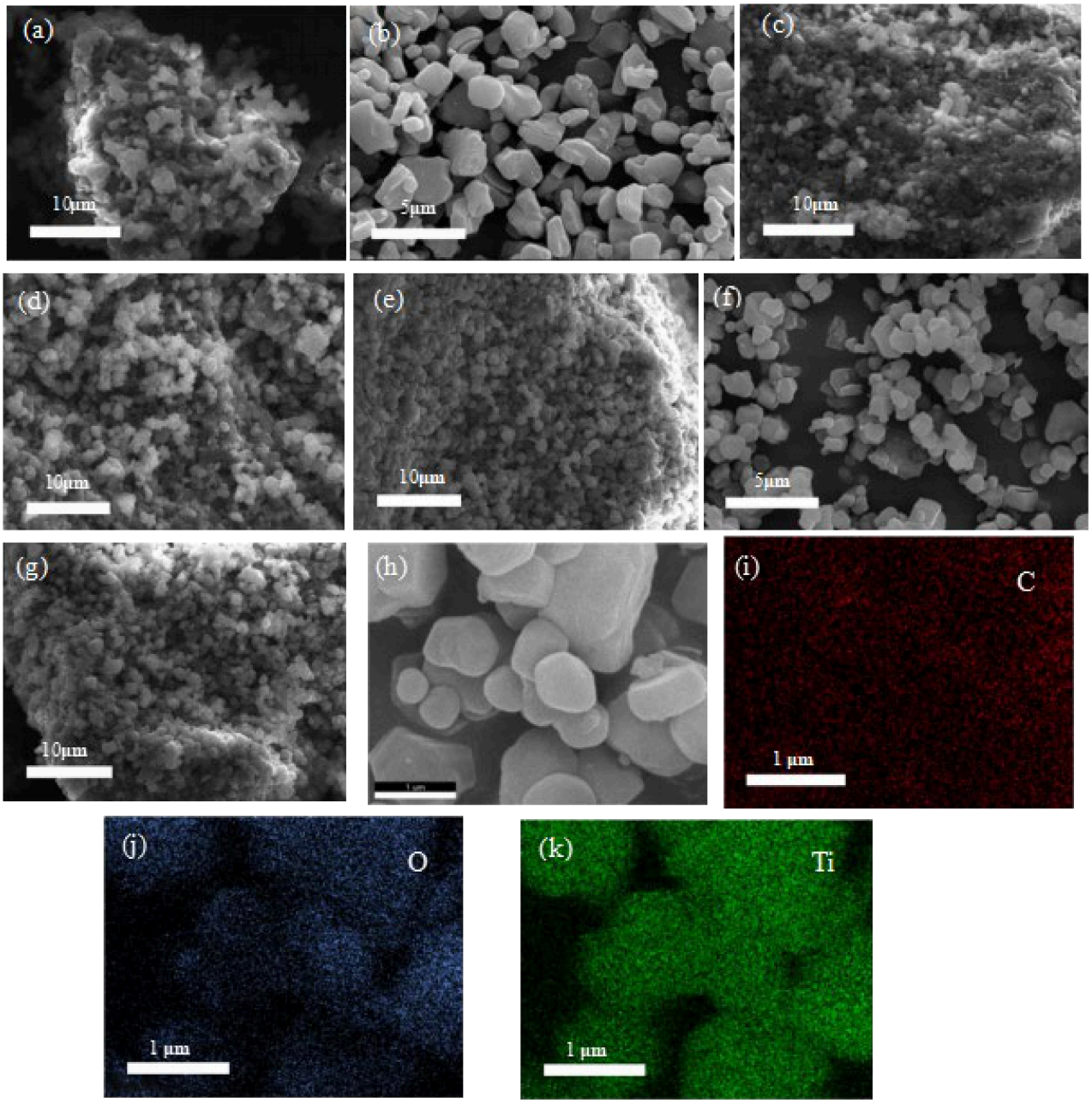


Figure 3. (**a**,**b**) SEM and FESEM images of LTO-0; (**c**,**d**) SEM images of LTO-1 and LTO-2; (**e**,**f**) SEM and FESEM images of LTO-3; (**g**) SEM images of LTO-4; (**h**) high-magnification SEM image of selected region of LTO-3 for EDS test; (**i**–**k**) EDS elemental mapping of C, O and Ti for LTO-3.

Combined analysis of Figure 3c–g reveals that with increasing dopant loading, the surface microstructure of LTO-n undergoes continuous evolution: the grain contours become progressively clearer and more regular, and an ordered porous structure is gradually constructed on the surface. For LTO-1 and LTO-2, although pores are formed on the surface, their number is relatively limited and the pore channels are not well developed. LTO-3 exhibits more abundant and uniformly distributed surface pores. A comparison of Figure 3b,f (FESEM images) shows that the modified LTO-3 particles are significantly smaller and more uniform than those of LTO-0, which is beneficial for subsequent adsorption. However, at excessively high doping levels (LTO-4), pronounced particle agglomeration occurs. Such agglomeration can shield a large number of surface active sites, hindering the contact

between lithium ions in the liquid phase and ion-exchange sites, thereby compromising the adsorption performance.

EDS elemental mapping analysis was performed on a selected region of LTO-3 (Figure 3h), and the corresponding elemental distributions of C, O, and Ti are shown in Figure 3i–k. The C, O, and Ti elements are uniformly dispersed throughout the matrix without significant elemental segregation or localized enrichment, indicating that carbon has been successfully and homogenously introduced into the lithium titanate crystal system. The overall morphological results confirm that LTO-3 at this doping ratio possesses the optimal mesoporous structure and crystalline state, and this conclusion is consistent with the XRD phase analysis results.

Figure 4a presents the FT-IR spectra of LTO-0 and LTO-3. The broad absorption bands in the range 3426.8–3430.7 cm^{-1} are attributed to the O-H stretching vibrations of adsorbed water molecules and Ti-OH hydroxyl groups on the sample surface, while the bands at 1627.6–1629.5 cm^{-1} correspond to the H-O-H bending vibrations of adsorbed water [31]. The absorption peaks at 863.9–867.8 cm^{-1} and 688.4 cm^{-1} are assigned to the Ti-O stretching vibrations of $[TiO_6]$ octahedra within the Li_2TiO_3 lattice and the Ti-O-Li lattice vibrations, which are characteristic intrinsic absorption peaks of Li_2TiO_3. In contrast to LTO-0 (prepared without organic additives), LTO-3 exhibits multiple additional absorption peaks in the 1030–1440 cm^{-1} region. The peaks at 1035.5 cm^{-1} and 1116.5 cm^{-1} are attributable to the C-O single-bond vibrations of oxygen-containing carbon species (including ether linkages, alcoholic hydroxyl groups, and carboxylates) that remain on the particle surface as a result of oxidative decomposition of polyacrylic acid and P188 during the calcination process. These residual hydrophilic groups substantially enhance the hydrophilicity of the sample, thereby facilitating subsequent acid washing and adsorption processes.

The TG-DTG-DSC thermal analysis curves of LTO-3 are shown in Figure 4b. For the sample pre-dried at 100 °C, the thermal decomposition process can be divided into four stages. In the temperature range from room temperature to 200 °C, the sample exhibits a weight loss of 10.1%, which is mainly attributed to the removal of residual ethanol and adsorbed water from the precursor, along with intramolecular dehydration of polyacrylic acid molecules. In the 200–350 °C range, a mass loss of 7.7% is observed, corresponding to the initial decarboxylation and decomposition of polyacrylic acid, accompanied by the onset of thermal oxidation of the P188 molecular chains. The 350–450 °C range shows a maximum weight loss of 46.2%, with a sharp decomposition peak in the DTG curve and a pronounced exothermic signal in the DSC curve. This stage corresponds to the vigorous oxidative combustion of the major components of polyacrylic acid and the surfactant P188, during which a large proportion of the organic components decompose and are removed as gaseous products. The gas evolution also leaves behind extensive porous structures within the material. In the 450–900 °C range, only a slight continuous weight loss of 3.1% is observed, indicating that the organic additives have been largely decomposed. At this stage, the lithium and titanium inorganic salt precursors undergo solid-state reactions and gradually crystallize to form Li_2TiO_3. The minor weight loss can be attributed to the further oxidation of residual carbon and the ordering of the lattice structure. These thermogravimetric results demonstrate that LTO-3 possesses excellent thermal stability.

X-ray photoelectron spectroscopy (XPS) was employed to analyze the elemental composition and chemical bonding states of the samples LTO-0 and LTO-3. As shown in Figure 4c, the XPS survey spectra reveal that the surface regions of the samples are mainly composed of four elements, C, O, Ti, and Li, indicating that no significant impurities were introduced during the preparation process and the sample surfaces are relatively clean. In Figure 4d, the Ti $2p_1/_2$ and Ti $2p_3/_2$ peaks of LTO are located at 463.88 and 458.18 eV, respectively, confirming that the chemical state of Ti is Ti(IV) [31]. Meanwhile, with the introduction

of polyacrylic acid, the Ti $2p_1/_2$ peak of LTO-3 shifts to 463.75 eV, shifting slightly toward lower binding energy. This suggests that the chemical environment of Ti^{4+} has been altered, which is likely attributable to the coordination between the carboxyl groups of polyacrylic acid and Ti^{4+} ions, thereby influencing the electron cloud density of Ti^{4+}.

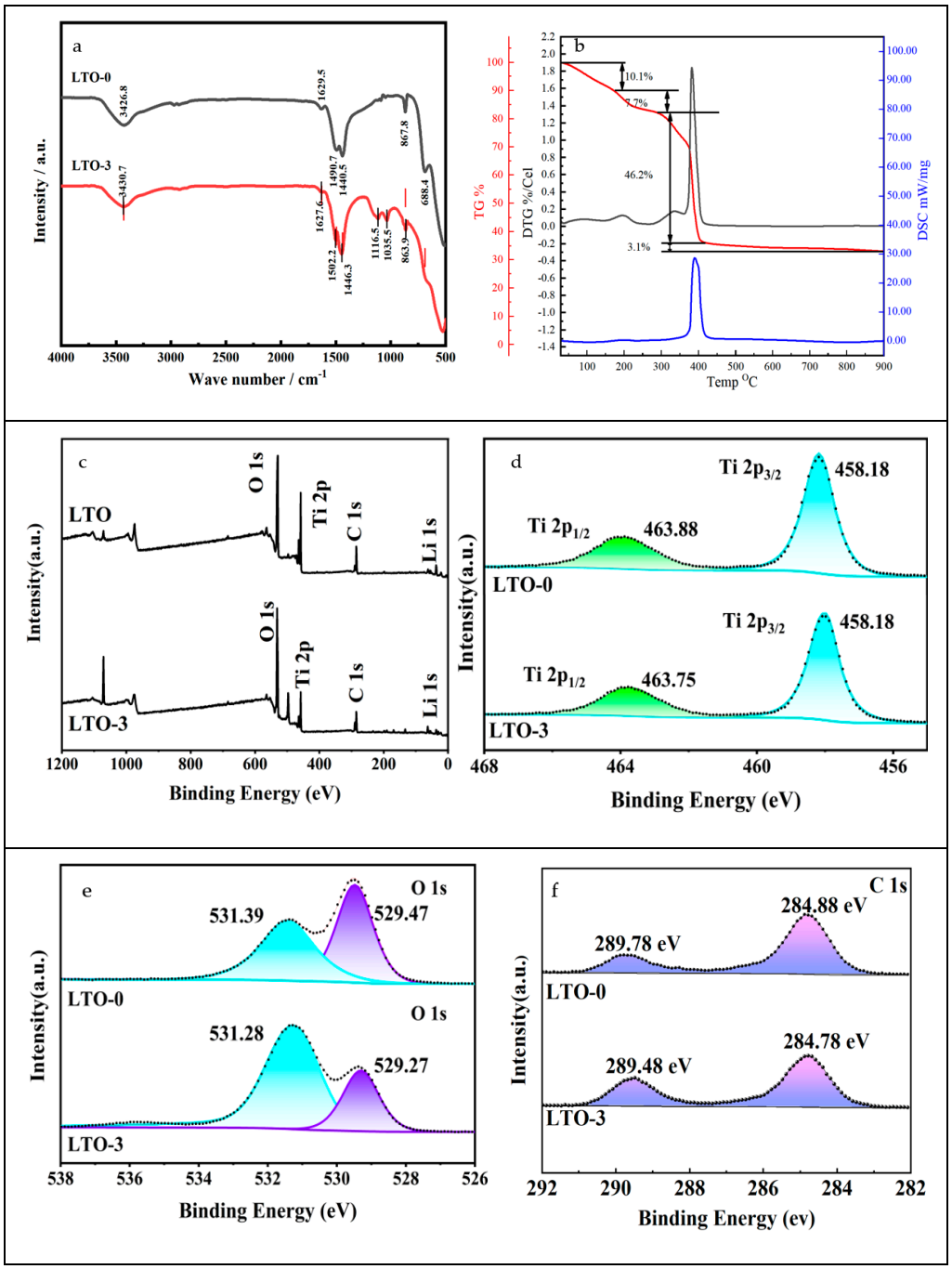


Figure 4. (**a**) FTIR spectra of LTO-0 and LTO-3 samples; (**b**) TG-DTG-DSC curves for LTO-3 sample; (**c**) XPS survey of LTO-0 and LTO-3; (**d**) Ti 2p, (**e**) O 1s and (**f**) C 1s high-resolution XPS spectra.

The O 1s spectra of LTO-0 and LTO-3 are presented in Figure 4e. LTO-0 exhibits two O 1s characteristic peaks at 531.39 and 529.47 eV, while LTO-3 shows corresponding peaks at 531.28 and 529.27 eV. These two peaks are assigned to surface hydroxyl groups (-OH) and lattice oxygen (O^{2-}), respectively [31]. The shift in the oxygen peaks in LTO-3 toward lower binding energy may be attributed to the chemical bonding between the carboxylate groups

(-COO^-) in the polyacrylic acid chains and the titanium-oxygen framework. The strong electronegativity of these groups induces an increase in the electron cloud density of lattice oxygen, thereby reducing the O^{2-} binding energy. In addition, the amorphous carbon layer derived from the pyrolysis of P188 that covers the material surface, along with the charge transfer effects of sp^2/sp^3 hybridized carbon, may also contribute to the apparent binding energy shifts.

The C 1s XPS spectra of both LTO-0 and LTO-3 were deconvoluted into two characteristic peaks (Figure 4f). The signals near 284.8 eV are assigned to C-C/C-H type carbon species, while the peaks at approximately 289.5 eV correspond to oxygen-containing carbon species, including C-O and carboxyl groups. Compared with the control sample LTO-0, the carbon peaks of LTO-3 prepared with polyacrylic acid and P188 show slight binding energy shifts. This can be explained by the thermal oxidative decomposition of polyacrylic acid and P188 during the high-temperature calcination stage, during which most of the organic components are removed as gaseous products, while a small amount of pyrolytic carbonaceous intermediates remain on the surface of the Li_2TiO_3 particles. The residual carbon species, which contain abundant oxygen-containing functional groups, interact with the matrix surface at the interface, altering the electronic environment around the carbon atoms. This ultimately results in the shift in the C 1s characteristic peaks and an increase in the relative content of oxygen-containing carbon components.

The pore structure characteristics and specific surface areas of HTO-0 and HTO-3 were characterized by N_2 adsorption–desorption isotherms (Figure 5). According to the IUPAC classification, both materials exhibit typical type IV adsorption isotherm features. As shown in Figure 5b, the isotherm of HTO-3 displays a pronounced hysteresis loop when the relative pressure (P/P_0) exceeds 0.4, indicating that the material is a typical mesoporous material [43]. The inset in Figure 5b reveals that the mesopores of HTO-3 are mainly concentrated at pore sizes of approximately 2.5 nm and 40 nm. In contrast, Figure 5a shows that the pores of HTO-0 are predominantly distributed at 60 nm and 1.8 nm, with a highly non-uniform particle size distribution.

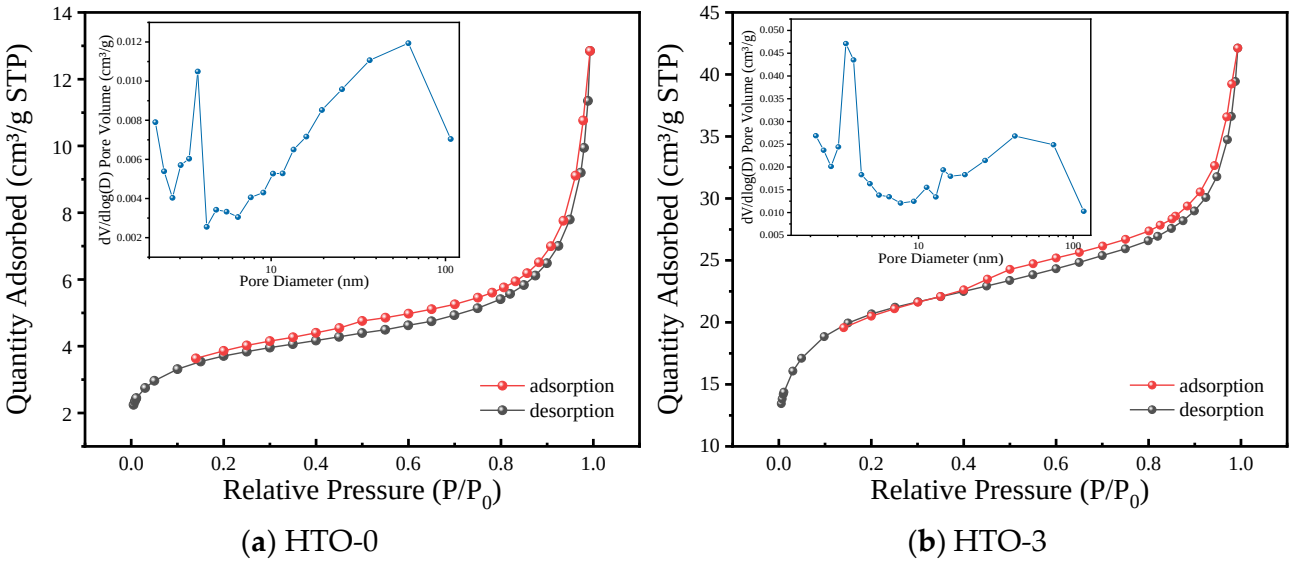


Figure 5. N_2 adsorption–desorption isotherms and pore size distribution of HTO-0 and HTO-3.

As summarized in Table 1, after modification with polyacrylic acid and P188, the specific surface area of H_2TiO_3 increased significantly from 12.35 m^2/g to 67.28 m^2/g. This substantial increase provides a larger solid–liquid contact interface and exposes more active sites, which facilitates the mass transfer of Li^+ between the solution and the adsorbent

surface. Pore size distribution analysis further reveals that the average pore diameter of the modified sample decreased from 6.44 nm to 3.87 nm, while the pore volume increased from 0.0022 cm^3/g to 0.0163 cm^3/g. The number of mesopores is markedly increased and the particles are more uniform. These structural changes arise from the gradual in-situ carbonization of polyacrylic acid and P188 during high-temperature calcination, which forms amorphous carbon that restricts the growth of Li_2TiO_3 crystals to the nanoscale and ensures their uniform dispersion within the carbon framework. This ultimately yields Li_2TiO_3@C composites with high specific surface area, large pore volume, uniform pore size, and nanoscale dimensions. The increased specific surface area enhances the hydrophilicity of the material and accelerates the mass transfer of lithium ions, thereby improving its adsorption capacity.

Table 1. Porous properties (BET surface area, pore volume, pore diameter) of samples.

Sample	Surface Area (m^2/g)	Pore Volume (cm^3/g)	Pore Diameter (nm)
HTO-0	12.35	0.0022	6.44
HTO-3	67.28	0.0163	3.87

3.3. Adsorption Experiments

3.3.1. Effects of Chelating Agent Mass Ratio and pH Value on Adsorption Capacity

To investigate the effect of chelating agent mass ratio on adsorption performance, the adsorption capacities of ion sieves HTO-0 to HTO-4 were measured, and the results are shown in Figure 6a. The adsorption capacities of HTO-0 through HTO-4 were 29.94, 31.23, 33.23, 36.03, and 32.16 $mg \cdot g^{-1}$, respectively. Among these, the HTO-3 sample exhibited the highest adsorption capacity, while the capacity of HTO-4 decreased. This decline is likely attributable to the collapse of the framework structure and blockage of pore channels caused by excessive chelating agent dosage during pyrolysis. Therefore, LTO-3 was determined to be the optimal doping level, which is consistent with the aforementioned XRD, SEM, and BET analyses.

In addition, to explore the influence of solution pH on adsorption performance, the lithium adsorption characteristics of the HTO-3 ion sieve were investigated at 298 K over a pH range of 4, 7, 10, 11, and 12. The experimental data (Figure 6b) indicate that the lithium adsorption capacity increases with increasing pH of the solution, suggesting that an alkaline environment is more favorable for the adsorption process. When the solution pH was increased to 12, the equilibrium adsorption capacity of HTO-3 reached a maximum of 36.03 $mg \cdot g^{-1}$. This is because the adsorption by the HTO ion sieve proceeds through the ion exchange between Li^+ and H^+ ($[H]_2TiO_3(s) + 2Li^+(aq) \leftrightarrow [Li]_2TiO_3(s) + 2H^+(aq)$). An increase in OH^- concentration facilitates the removal of H^+ from the crystal lattice and the transfer of Li^+, thereby promoting the adsorption capacity [33]. Considering that the adsorption capacity varies with solution pH during the adsorption process, a buffer solution at pH = 12 was used in subsequent experiments to maintain system stability.

3.3.2. Adsorption Isotherms and Adsorption Thermodynamics

The adsorption capacity of HTO-3 was measured at 298 K using different initial Li^+ concentrations ranging from 100 to 450 $mg \cdot L^{-1}$. To analyze the adsorption behavior of Li^+ on the surface of HTO-3, the Langmuir and Freundlich isotherm models were employed to fit the equilibrium adsorption data, allowing for a preliminary determination of the adsorption mode. The results are presented in Figure 6c,d. The theoretical maximum equilibrium adsorption capacity (Q_m) calculated from the Langmuir model was 38.43 $mg \cdot g^{-1}$. The correlation coefficient (R^2) of the Langmuir model (0.9953) was higher than that of

the Freundlich model (0.9827), as summarized in Table 2, indicating that the Langmuir model can more accurately describe the adsorption of Li^+ onto HTO-3, confirming that the adsorption proceeds via a monolayer adsorption process.

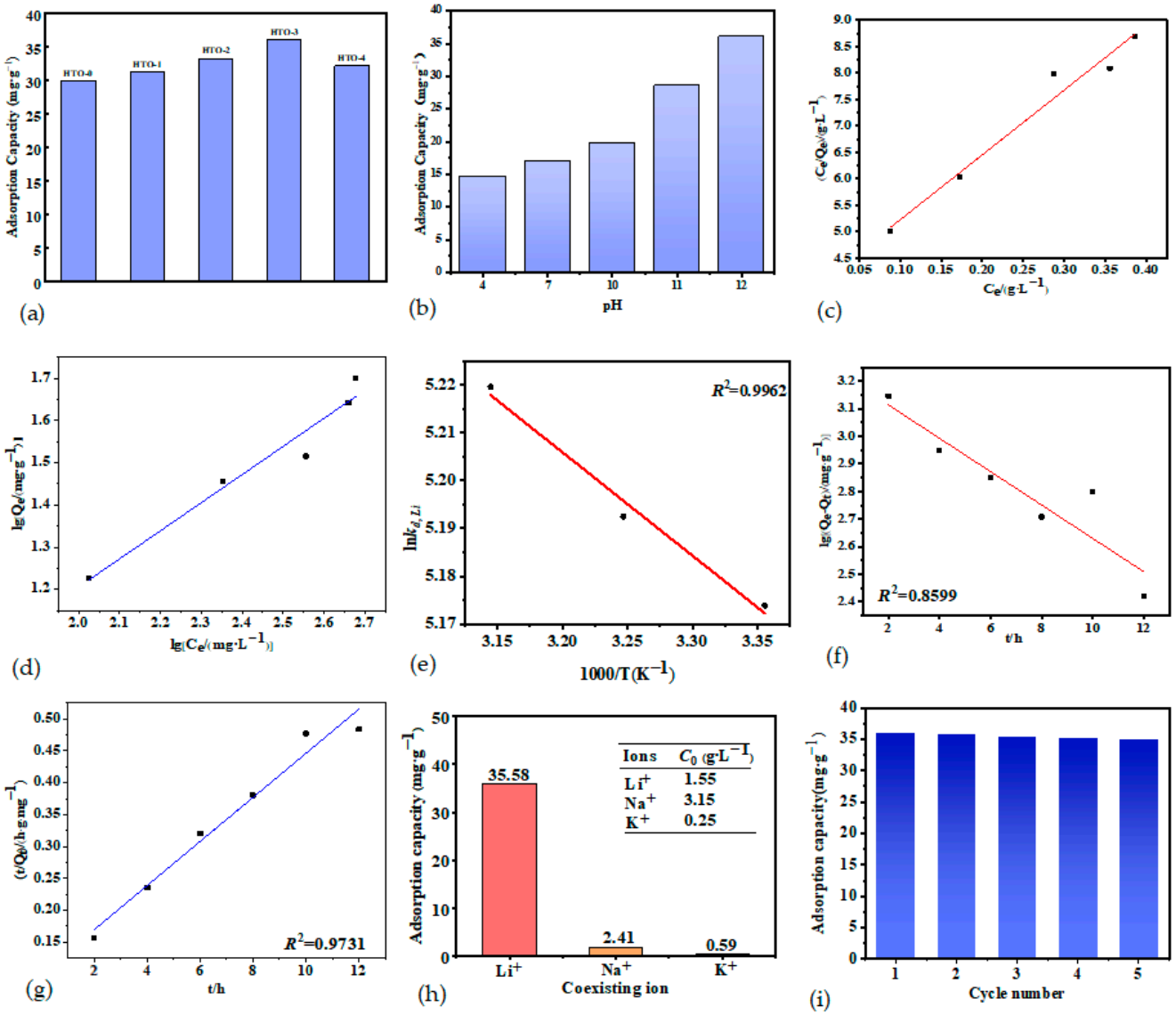


Figure 6. (**a**) Lithium adsorption capacities of HTO-n; (**b**) effect of pH on the lithium adsorption capacity of HTO-3; (**c**) Langmuir and (**d**) Freundlich adsorption isotherms for Li^+ adsorption; (**e**) thermodynamic fitting plot for Li^+ adsorption on HTO-3; (**f**) linear fitting of pseudo-first-order kinetic model and (**g**) pseudo-second-order kinetic model; (**h**) adsorption selectivity of HTO-3; (**i**) Cycling performance of HTO-3 for Li^+ adsorption.

Table 2. Fitting parameters of adsorption isotherm models for the adsorbent.

Langmuir			Freundlich		
Q_m/mg·g^{-1}	K_L/L·mg^{-1}	R^2	n	K_F/L·g^{-1}	R^2
38.43	0.0030	0.9953	1.5771	1.0536	0.9827

Adsorption thermodynamics describes the inherent energy changes and underlying mechanisms during the adsorption process. At the same initial Li^+ concentration, the adsorption capacities at 298, 308, and 318 K were 36.03, 38.13, and 40.97 mg·g^{-1}, respectively.

The corresponding distribution coefficients $K_{d,Li}$ were 122.11, 150.65, and 189.45 mL·g^{-1}, respectively. The plot of ln $K_{d,Li}$ as a function of temperature $(1000/T)$ is shown in Figure 6e, and the thermodynamic parameters are listed in Table 3. The adsorption enthalpy (ΔH) was determined to be 16.05 kJ·mol^{-1}, indicating that the adsorption process is endothermic. When ΔH close to 16 16 kJ·mol^{-1}, it suggests that lithium adsorption is governed by ion exchange [34]. The entropy change (ΔS) was 102.4 J·mol^{-1}·K^{-1}. This entropy increase arises from the difference in hydration shell structures between Li^+ and H^+: the exchange process $Li^+(H_2O)_4 \rightarrow H^+(H_2O) + 3H_2O$ [17] leads to an increase in the degree of freedom of the system. The negative values of ΔG indicate that the ion exchange between Li^+ and H^+ in HTO-3 is a spontaneous process. Furthermore, the absolute value of ΔG increases with rising temperature. This trend in the endothermic adsorption process can be attributed to the accelerated migration rate of Li^+ at higher temperatures, which significantly enhances the probability of contact between Li^+ and HTO-3 [35]. As the temperature increases, the spontaneity of the adsorption process is strengthened, ultimately leading to an improvement in adsorption capacity.

Table 3. Thermodynamic parameters of lithium adsorption on HTO-3.

ΔH (kJ·mol^{-1})	ΔS (J·mol^{-1}·K^{-1})	ΔG (kJ·mol^{-1})		
16.05	102.4	298 K	308 K	318 K
		−14.4652	−15.4892	−16.5132

3.3.3. Adsorption Kinetics

To investigate the adsorption kinetic characteristics of the HTO-3 material, the adsorption capacity of 0.1 g of HTO-3 was measured in 100 mL of LiCl solution (C_{Li+} = 200 mg·L^{-1}) at 298 K. The pseudo-first-order and pseudo-second-order kinetic models were employed to analyze the adsorption process. The adsorption capacities at different time intervals were determined, and the data were linearly fitted using the two kinetic equations, respectively. The corresponding fitting curves are presented in Figure 6f,g, and the calculated fitting parameters are summarized in Table 4. The correlation coefficient (R^2) for the pseudo-first-order kinetic model was 0.8599, whereas that for the pseudo-second-order model was 0.9731. The better linear fit of the pseudo-second-order model indicates that the adsorption process of the modified lithium-ion sieve follows pseudo-second-order kinetics, suggesting that chemisorption is the rate-controlling step [31].

Table 4. Kinetic parameters for Li^+ adsorption on HTO-3.

Sample	Q_e/(mg·g^{-1})	Pseudo-First-Order		Pseudo-Second-Order	
		k_1/h	R^2	k_2/(g·mg^{-1}·h^{-1})	R^2
HTO-3	39.13	0.06052	0.8599	0.011925	0.9731

3.3.4. Adsorption Selectivity and Cyclic Performance

Adsorption experiments were conducted using HTO-3 in a simulated brine containing Li^+, Na^+, and K^+ at concentrations of 1.55, 3.15, and 0.25 g·L^{-1}, respectively. As shown in Figure 6h, the lithium adsorption capacity reached 35.58 mg·g^{-1}, which is close to that in pure lithium solution (36.03 mg·g^{-1}), indicating that the coexisting ions have a weak effect on the lithium adsorption of HTO-3. The calculated distribution coefficients (K_d) for Li^+, Na^+, and K^+ were 23.5, 0.77, and 2.37 mL·g^{-1}, respectively, and the separation factors of Li^+/Na^+ and Li^+/K^+ were 30.52 and 9.92, respectively. These results further confirm that HTO-3 exhibits high selectivity toward Li^+.

Since lithium-ion sieves can be regenerated through adsorption and acid-washing processes, their cyclic performance is a crucial indicator for practical applications. For HTO-3, the variation in adsorption capacity over five cycles is clearly presented in Figure 6i. After five cycles, the adsorption capacity decreased slightly from the initial value of 36.03 $mg \cdot g^{-1}$ to 34.91 $mg \cdot g^{-1}$, with a retention rate of 96.9%. This result demonstrates that the lithium-ion sieve exhibits good stability during the adsorption–desorption cycling process. The slight decline in adsorption capacity can be attributed to the inevitable lattice contraction caused by repeated ion exchange during cycling, which, to some extent, affects the adsorption capacity [30].

4. Conclusions

In this study, Li_2TiO_3 mesoporous carbon composites (Li_2TiO_3@C) were successfully fabricated via a molecular design strategy involving the co-assembly of Ti^{4+}/Li^{+}-polyacrylate chelates with Poloxamer 188. Innovatively, polyacrylic acid was employed as a ligand to design Ti^{4+}/Li^{+}-polyacrylate chelates as novel molecular precursors. Through the chelation of carboxyl groups in polyacrylate with titanium and lithium, stoichiometric coordination of Li^{+} and Ti^{4+} was achieved uniformly at the molecular scale, ensuring the homogeneous dispersion of Li^{+} and Ti^{4+} precursors and laying the foundation for the synthesis of materials with uniform mesoporous structures. The hydroxyl functional groups in the polymer ligand formed strong hydrogen bonds with the poly(ethylene oxide) (PEO) segments of the Poloxamer 188 template, and such interactions guided the formation of well-developed mesoporous structures.

Experimental results demonstrated that the ion sieve HTO-3, prepared at a theoretical mass ratio of Li_2TiO_3 to polyacrylic acid to Poloxamer 188 of 1:2:0.3, exhibited the optimal lithium adsorption performance. The specific surface area of the modified HTO-3 increased to 67.28 m^2/g, representing an increase of 54.93 m^2/g compared with the unmodified ion sieve. At pH = 12 and 298 K, the equilibrium adsorption capacity reached 36.03 $mg \cdot g^{-1}$, which was 6.09 $mg \cdot g^{-1}$ higher than that of HTO-0. The adsorption capacity retention of HTO-3 after five cycles was 96.9%, indicating that the modified ion sieve exhibits high stability and can be reused over multiple cycles. Furthermore, the adsorption isotherms were better described by the Langmuir model, and the adsorption kinetics followed the pseudo-second-order model, suggesting that the adsorption process is chemisorption-dominated monolayer adsorption. This study provides a novel approach for constructing mesoporous lithium-ion sieves featuring small particle size, high specific surface area, large adsorption capacity, and excellent cyclic stability. Future work will focus on the granulation and shaping of the material and its implementation in industrial fixed-bed columns.

Author Contributions: Conceptualization, X.-Z.Z. and H.-B.L.; Methodology, T.-X.Z.; Validation, X.T. and G.-M.C.; Investigation, Y.-L.Q. and S.-Y.L.; Resources, L.-Y.Z.; Data curation, G.-M.C., S.-Y.L., Y.-L.Q. and X.T.; Writing—original draft, X.-Z.Z.; Supervision, L.-Y.Z., H.-B.L. and T.-X.Z.; Funding acquisition, L.-Y.Z. and H.-B.L. All authors have read and agreed to the published version of the manuscript.

Funding: This work is supported by grants from the Natural Science Foundation of Sichuan Province (General Program), Grant No. 2026NSFSC0348; Sichuan Province College Students Innovation and Entrepreneurship Training Program (Project Nos. X2025004, X2025001, X2026025).

Data Availability Statement: The original contributions presented in this study are included in the article. Further inquiries can be directed to the corresponding authors.

Conflicts of Interest: The authors declare that they have no conflicts of interest.

References

1. Tyrsa, V.; Burtseva, L. Generation of thermonuclear energy by fusing hydrogen and lithium atoms. *Tech. Phys.* **2003**, *48*, 807–812. [CrossRef]
2. Liu, Q.; Hu, Z.; Li, M.; Shi, X. Porous. Spherical Granulation of Co-Doped Manganese-Based Lithium Ion-Sieve with Solid Paraffin as Mesoporous Porogen for Lithium Recovery from Salt Lake Brine. *Separations* **2026**, *13*, 277. [CrossRef]
3. Zhao, S.; Yan, K.; Zhang, J.; Sun, B.; Wang, G. Reviving Reaction Mechanism of Layered Lithium-Rich Cathode Materials for High-Energy Lithium-Ion Battery. *Angew. Chem. Int. Ed.* **2021**, *60*, 2208–2220. [CrossRef] [PubMed]
4. Fu, X.; Zhong, W. Biomaterials for high-energy lithium-based batteries: Strategies, challenges, and perspectives. *Adv. Energy Mater.* **2019**, *9*, 1901774. [CrossRef]
5. Liu, Q.; Yu, X.; Huang, X. Effect of different arrangement on thermal runaway characteristics of 18,650 lithium-ion batteries under the typical pressure in civil aviation transportation. *Fire Technol.* **2020**, *56*, 2509–2523. [CrossRef]
6. Jung, M.; Mishra, B. Kinetic and thermodynamic study of aluminum recovery from the aluminum smelter baghouse dust. *J. Sustain. Metall.* **2016**, *2*, 257–264. [CrossRef]
7. Delgado, M.A.; Sánchez, M.C.; Valencia, C.; Franco, J.M.; Gallegos, C. Relationship among microstructure, rheology and processing of a lithium lubricating grease. *Chem. Eng. Res. Des.* **2005**, *83*, 1085–1092. [CrossRef]
8. Delgado, M.A.; Valencia, C.; Sánchez, M.C.; Franco, J.M.; Gallegos, C. Thermorheological behaviour of a lithium lubricating grease. *Tribol. Lett.* **2006**, *23*, 47–54. [CrossRef]
9. Huang, S.; Cao, P.; Wang, C.; Huang, Z.; Gao, W. Fabrication of a high-strength lithium disilicate glass-ceramic in a complex glass system. *J. Asian Ceram. Soc.* **2013**, *1*, 46–52. [CrossRef]
10. Ma, Y.; Han, Y.; Yang, Y.; Zhang, T.; Yao, J.; Li, Y.; Zong, Y.; Wang, W. Confinement-effect adsorbents based on titanium-based lithium ion sieve for efficient lithium adsorption under natural pH conditions. *Chem. Eng. J.* **2025**, *524*, 169208. [CrossRef]
11. Han, Z.; Qi, S.; Fu, M.; Han, L.; Hong, C.; Shen, Z.; Wang, X.; Su, K.; Xue, X.; Zhang, B.; et al. A Scalable Route to Constructing Hydrogel-Encapsulated Lithium-Ion Sieves-Based Photothermal Fabric Adsorbent for Solar-Enhanced Lithium Extraction from Seawater. *Adv. Funct. Mater.* **2025**, *35*, 2422901. [CrossRef]
12. Guo, Z.-Y.; Wang, J.; Zhang, P.; Wang, L.; Lai, Z.; Ji, Z.-Y. Lithium selective membranes for direct lithium extraction from complex brine. *Prog. Mater. Sci.* **2026**, *156*, 101582. [CrossRef]
13. Tabelin, C.B.; Dallas, J.; Casanova, S.; Pelech, T.; Bournival, G.; Saydam, S.; Canbulat, I. Towards a low-carbon society: A review of lithium resource availability, challenges and innovations in mining, extraction and recycling, and future perspectives. *Miner. Eng.* **2021**, *163*, 106743. [CrossRef]
14. Zhu, Z.; Jiang, Y.; Wang, Z.; Tian, Q.; Yue, X.; Zhang, T.; Qiu, F. Solar-driven high specific surface network membrane for efficient lithium recovery. *J. Chem. Technol. Biotechnol.* **2026**, *101*, 766–775. [CrossRef]
15. Zheng, L.; Chen, J.; Sun, J.; Liu, M.; Gao, Y.; Guo, Z. Highly selective lanthanide-doped ion sieves for lithium recovery from aqueous solutions. *J. Chem. Res.* **2023**, *47*, 1159051. [CrossRef]
16. Liu, L.; Kuang, Q.; Xu, S.; Pan, W.; Liu, Y.; Zhou, J.; Tang, A.; Xue, J. Enhanced lithium-ion adsorption by recyclable lithium manganese oxide-sepiolite composite microsphere from aqueous media: Fabrication, structure, and adsorption characteristics. *J. Mol. Liq.* **2023**, *380*, 121780. [CrossRef]
17. Jiang, H.; Zhang, S.; Yang, Y.; Yu, J. Synergic and competitive adsorption of Li-Na-$MgCl_2$ onto lithium-aluminum hydroxides. *Adsorption* **2020**, *26*, 1039–1049. [CrossRef]
18. Wang, S.; Zhang, M.; Zhang, Y.; Zhang, Y.; Qiao, S.; Zheng, S. High adsorption performance of the Mo-doped titanium oxide sieve for lithium ions. *Hydrometallurgy* **2019**, *187*, 30–37. [CrossRef]
19. Qian, J.; You, R.; Shen, C.; Xue, F.; Ju, S. Preparation of H_2TiO_3@GO for rapid adsorption of Li^+ and its adsorption behaviour. *Mater. Sci. Eng. B* **2024**, *302*, 117220. [CrossRef]
20. Xu, Y.; Peng, H.; Luo, H.; Zhang, Q.; Liu, Z.; Zhao, Q. High performance Mg^{2+}/Li^+ separation membranes modified by a bis-quaternary ammonium salt. *Desalination* **2022**, *526*, 115519. [CrossRef]
21. He, R.; Dong, C.; Xu, S.; Liu, C.; Zhao, S.; He, T. Unprecedented Mg^{2+}/Li^+ separation using layer-by-layer based nanofiltration hollow fiber membranes. *Desalination* **2022**, *525*, 115492. [CrossRef]
22. Huang, T.; Song, J.; He, S.; Li, T.; Li, X.-M.; He, T. Enabling sustainable green close-loop membrane lithium extraction by acid and solvent resistant poly(ether ether ketone) membrane. *J. Membr. Sci.* **2019**, *589*, 117273. [CrossRef]
23. Miao, J.; Zhao, K.; Guo, F.; Xu, L.; Xie, Y.; Deng, T. Novel LIS-doped mixed matrix membrane absorbent with high structural stability for sustainable lithium recovery from geothermal water. *Desalination* **2022**, *527*, 115570. [CrossRef]
24. Ding, X.-X.; Jiang, C.; Wang, J.-W.; Wu, Z.-H.; Luo, R.; Zhao, Y.; Wang, Y.; Shao, D.-D. Biomass-derived modifiers customize polymeric nanofiltration membranes for enhanced lithium/magnesium ion selectivity. *Desalination* **2026**, *625*, 119923. [CrossRef]
25. Xue, Z.; Zhang, P.; Zhang, Q.; Huang, C.; Wang, C.; Mao, L.; Zhou, X.; Ju, H.; Sun, J.; Shao, F.; et al. Lithium isotope separation by precipitation method coupled with solvent extraction with 1-Hydroxy-4-(p-toluidino)anthraquinone. *J. Mol. Liq.* **2023**, *391*, 123131. [CrossRef]

26. Zhang, Y.; Hu, Y.; Wang, L.; Sun, W. Systematic review of lithium extraction from salt-lake brines via precipitation approaches. *Miner. Eng.* **2019**, *139*, 105868. [CrossRef]
27. Guan, J.; Zhou, Z.; Li, N.; Liu, Z.; Wen, H.; Li, J.; Hu, L.; Liu, L.; Luo, C. Extracting lithium from the H_2SO_4 leaching solution of bauxitic claystone via co-precipitation methods without addition of Al source. *Chem. Eng. J. Adv.* **2022**, *9*, 100223. [CrossRef]
28. Coterillo, R.; Gallart, L.-E.; Fernández-Escalante, E.; Junquera, J.; García-Fernández, P.; Ortiz, I.; Ibañez, R.; San-Román, M.-F. Selective extraction of lithium from seawater desalination concentrates: Study of thermodynamic and equilibrium properties using Density Functional Theory (DFT). *Desalination* **2022**, *532*, 115704. [CrossRef]
29. Pu, X.; Du, X.; Jing, P.; Wei, Y.; Wang, G.; Xian, C.; Wu, K.; Wu, H.; Wang, Q.; Ji, X.; et al. Interface and defect engineering enable fast and high-efficiency Li extraction of metatitanic acid adsorbent. *Chem. Eng. J.* **2021**, *425*, 130550. [CrossRef]
30. Liu, Q.; Xing, H.; Zhang, Y.; Zhao, Y.; Rong, M.; Liu, H.; Yang, L. Highly hydrophilic H_2TiO_3 ion sieve with neodymium (Nd) doping enables fast and high-efficiency Li extraction. *Sep. Purif. Technol.* **2024**, *345*, 127263. [CrossRef]
31. Zhang, H.; Dong, B.; Yang, Y.; Long, X.; Chen, H.; Pan, J.; Zhou, C. Cu-doped titanium lithium-ion sieves with cell expansion and improved hydrophilicity for efficient extraction of lithium from aqueous resources. *Chem. Eng. J.* **2024**, *495*, 153545–153554. [CrossRef]
32. Deng, Y.; Chai, G.; Zhang, Y. Research progress on lithium extraction from salt-lake brine. *J. Ind. Eng. Chem.* **2025**, *148*, 92–108. [CrossRef]
33. Perez-Antolin, D.; Irastorza, C.; Gonzalez, S.; Moreno, R.; García-Quismondo, E.; Palma, J.; Lado, J.J.; Ventosa, E. Regenerative electrochemical ion pumping cell based on semi-solid electrodes for sustainable Li recovery. *Desalination* **2022**, *533*, 115764. [CrossRef]
34. Liu, D.; Zhao, Z.; Xu, W.; Xiong, J.; He, L. A closed-loop process for selective lithium recovery from brines via electrochemical and precipitation. *Desalination* **2021**, *519*, 115302. [CrossRef]
35. Song, Z.; Wu, X.; He, Q.; Huyan, J.; Gao, R.; Wu, X.; Miao, Z. Titanium ion sieves utilize flow electrode capacitive deionization technology to achieve efficient lithium extraction. *Sep. Purif. Technol.* **2026**, *392*, 137065. [CrossRef]
36. Orooji, Y.; Nezafat, Z.; Nasrollahzadeh, M.; Shafiei, N.; Afsari, M.; Pakzad, K.; Razmjou, A. Recent advances in nanomaterial development for lithium ion-sieving technologies. *Desalination* **2022**, *529*, 6–8. [CrossRef]
37. Chung, W.-J.; Torrejos, R.E.C.; Park, M.J.; Vivas, E.L.; Limjuco, L.A.; Lawagon, C.P.; Parohinog, K.J.; Lee, S.-P.; Shon, H.K.; Kim, H.; et al. Continuous lithium mining from aqueous resources by an adsorbent filter with a 3D polymeric nanofiber network infused with ion sieves. *Chem. Eng. J.* **2017**, *309*, 49–62. [CrossRef]
38. Wang, Q.; Yang, X.; Li, C.; Zhao, C.; Huang, Y.; Qiu, S.; Qin, Y.; Shi, C. Titanium-based lithium ion sieve adsorbent H_2TiO_3 with enhanced Li^+ adsorption properties by magnetic Fe doping. *Sep. Purif. Technol.* **2024**, *346*, 127455. [CrossRef]
39. Liu, E.; Luo, H.; Jiao, N.; Zhang, W.; Zhou, X.; Wu, L.; Yao, H.; Liang, X.; Liu, H. Enhancing the stability of Mn-based ion sieves via high-valence W doping for efficient lithium recovery from seawater. *Sep. Purif. Technol.* **2026**, *391*, 137110. [CrossRef]
40. Wu, W.; Chen, Z.; Wang, H.; An, X.; Cao, L.; Gao, J.; Chen, Y. Superhydrophilic photothermal adsorption material for efficient lithium extraction from seawater enhanced by synergistic effect of photovaporization and adsorption. *Sep. Purif. Technol.* **2026**, *387*, 136655. [CrossRef]
41. Chen, M.; Trivedi, J.; Zou, C.; Xia, L. Advances in lithium recovery from complex and dilute brines: A comprehensive review. *Can. Metall. Q.* **2026**, *65*, 3336–3353. [CrossRef]
42. Lin, Y.; Li, M.; Wang, S.; Xue, F.; Ju, S. Fabrication of biomass carbonaceous aerogel-modified ion sieve composites for lithium adsorption. *Mater. Lett.* **2024**, *363*, 136250. [CrossRef]
43. Wu, J.; Wang, W.; Chen, W.; Liu, C.; Deng, T.; Yu, X. Inorganic porous carbon as the supporter of H_2TiO_3 via in-situ polymerization synchronous conversion for lithium recovery from aqueous solutions. *Sep. Purif. Technol.* **2025**, *356*, 129806. [CrossRef]
44. Chen, X.; Shao, Y.; Xing, L.; Wei, Y.; Zhang, X. High specific surface area of H_2TiO_3 ion sieve for efficient lithium extraction from liquid resources. *Desalination* **2026**, *620*, 119601. [CrossRef]
45. Qin, W.; Xu, J.; Wei, X.; Han, J. Surface modification and spatial optimization of pre-lithiation TiO_2 ion sieves for efficient extraction of lithium. *Chem. Eng. J.* **2024**, *495*, 153401. [CrossRef]
46. Yang, Y.; Long, X.; Zhang, H.; Dong, B.; Chen, H.; Zhang, L.; Shi, S.; Zhou, C. Surface modification of lithium-ion sieves by silane coupling agent for improved adsorption performance. *Sep. Purif. Technol.* **2024**, *330*, 125422. [CrossRef]
47. Wang, C.; Wan, X.; Duan, L.; Zeng, P.; Liu, L.; Guo, D.; Xia, Y.; Elzatahry, A.A.; Xia, Y.; Li, W.; et al. Molecular Design Strategy for Ordered Mesoporous Stoichiometric Metal Oxide. *Angew. Chem. Int. Ed.* **2019**, *58*, 15863–15868. [CrossRef] [PubMed]
48. Wang, C.; Zhang, W.; Liu, M.; Duan, L.; Ma, B.; Zhang, X.; Li, W. Synthesis of $LiTiO_2$ Nanocrystals/Ordered Mesoporous Carbon Composite Hosts for High-Performance Lithium-Sulfur Batteries. *Small Sci.* **2023**, *3*, 2300019. [CrossRef] [PubMed]
49. Zhao, K.; Li, J.; Yuan, J.; Yu, X.; Guo, Y.; Jiang, Z.; Li, M.; Duo, J.; Deng, T. A novel Co-doped H_2TiO_3 spinning composite for efficient lithium recovery from alkaline lithium precipitation mother liquor. *Chem. Eng. J.* **2024**, *482*, 148989. [CrossRef]
50. Febriana, S.; Riyanto, E.S.; Dimyati, A.; Handayani, A. Characterization Studies of Cyclotron CS-30 Carbon Puller Material Using Powder X-Ray Diffraction and SEM, EDX Cross Section Method. *IOP Conf. Ser. Mater. Sci. Eng.* **2018**, *299*, 012054. [CrossRef]

51. Zhou, S.; Guo, X.; Yan, X.; Chen, Y.; Lang, W. Zr-doped titanium lithium ion sieve and EP-granulated composite: Superb adsorption and recycling performance. *Particuology* **2022**, *69*, 100–110. [CrossRef]
52. Ivanets, A.; Bicheva, E.; Kouznetsova, T.; Silerio-Vázquez, F.d.J.; Torsykbayeva, B.; Hosseini-Bandegharaei, A. Enhanced adsorption of Li^+ ion on Zr-doped $Li_4Ti_5O_{12}$ and Li_2TiO_3 oxides. *Sep. Purif. Technol.* **2025**, *374*, 133645. [CrossRef]

Disclaimer/Publisher's Note: The statements, opinions and data contained in all publications are solely those of the individual author(s) and contributor(s) and not of MDPI and/or the editor(s). MDPI and/or the editor(s) disclaim responsibility for any injury to people or property resulting from any ideas, methods, instructions or products referred to in the content.